ACS APPLIED ENERGY MATERIALS

www.acsaem.org Article

Polymer-Stabilized Liquid Metal Nanoparticles as a Scalable Current Collector Engineering Approach Enabling Lithium Metal Anodes

Tong Liu, Xinsheng Wu, Shang Zhu, Francesca Lorandi, Longchang Ni, Sipei Li, Mingkang Sun, Brian P. Bloom, David H. Waldeck, Venkatasubramanian Viswanathan,* Jay F. Whitacre,* and Krzysztof Matyjaszewski*

Cite This: ACS Appl. Energy Mater. 2022, 5, 3615−3625 Read Online

ABSTRACT: Dendrites and dead lithium formation over prolonged cycling have long been challenges that hinder the safe implementation of metallic Li anodes. Herein, we employ polymer-stabilized liquid metal nanoparticles (LM-P NPs) of eutectic gallium indium (EGaIn) to create uniform Li nucleation sites enabling homogeneous lithium electrodeposition. Block copolymers of poly(ethylene oxide) and poly(acrylic acid) (PEO-*b*-PAA) were grafted onto the EGaIn surface, forming stabilized, well-dispersed NPs. Using a scalable spray coating approach, LM-P NPs were fabricated on copper current collectors, providing lithiophilic PEO sites and interactive carboxyl groups to guide Li deposition. The Li-EGaIn alloying process greatly reduced the Li^+ diffusion barrier, enabling fast Li transport through the coating layer, resulting in decreased nucleation overpotential. Therefore, about five times lower Li nucleation overpotential was obtained on the LM-P modified Cu with an optimal composition of the polymers than the bare Cu substrates. DFT computations was used to reveal the binding properties between the LM-P layer and Li. Due to the regulated Li plating/stripping process, as-obtained 30 μm Li anodes paired with $LiNi_{0.8}Co_{0.1}Mn_{0.1}O_2$ (NCM811) with a negative/positive electrode capacity (N/P) ratio ∼ 10 exhibited stable cycling performance at 0.5C for over 250 cycles, with an average Coulombic efficiency of 99.55%. Ultrathin Li (1 μm) anodes with an N/P ratio ∼ 0.6 were also demonstrated in Li||$LiFePO_4$ cells, which examined the stabilization of Li by LM-P NPs and monitored practical loadings of Li anodes that are close to anode-free systems.

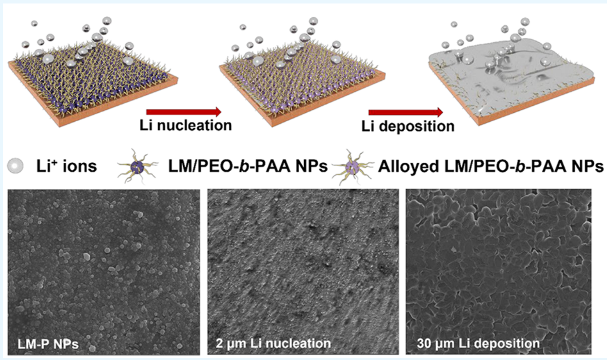

KEYWORDS: *lithium metal anode, eutectic alloys, block copolymers, ATRP, EGaIn, Cu current collector, liquid metal*

INTRODUCTION

Lithium metal anode batteries are regarded as one of the most promising next-generation high-energy-density batteries in the quest to find new solutions that outperform the state-of-the-art lithium-ion technology. The use of lithium metal as an anode is appealing due to its low reduction potential (−3.04 V vs the standard hydrogen electrode) and high specific capacity (3860 mAh g^{-1}), ease of manufacture, and potential use of alternate packaging technologies.[1−3] However, challenges must be overcome to enable the successful use of Li metal anodes.[4] One primary challenge is the formation of an unstable, native solid electrolyte interphase (SEI) on the surface of Li metal. The build-up of SEI during continuous cycling sequesters increasing amounts of fresh Li and electrolyte.[5−7] Additionally, Li trapped in SEI tends to disconnect from the electronically conductive framework during stripping, resulting in electrically isolated Li (i.e., "dead" Li). The Li consumption with formation of "dead" Li decreases the Coulombic efficiency (CE) and cycle life of Li metal batteries.[8] In addition, the nonuniform Li plating originating from localized charge concentration gradients at the Li/electrolyte interface contributes to the formation and growth of Li dendrites, which can pierce the separator and eventually reach the cathode, leading to internal short circuits, along with severe safety hazards.[9,10]

To overcome these barriers, various strategies have been developed,[11−15] including implementing structured/dimensional electrode designs,[16−22] engineering the surface of Li with an artificial SEI,[23−30] liquid electrolyte modification to achieve different interfacial qualities,[31−35] and solid-state electrolyte implementation.[36−41] Although remarkable progress has been achieved in stabilizing Li anodes, excess Li (typically 450−750 μm thick Li electrodes, corresponding to

Received: December 29, 2021
Accepted: March 2, 2022
Published: March 14, 2022

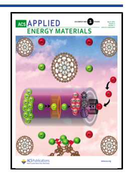

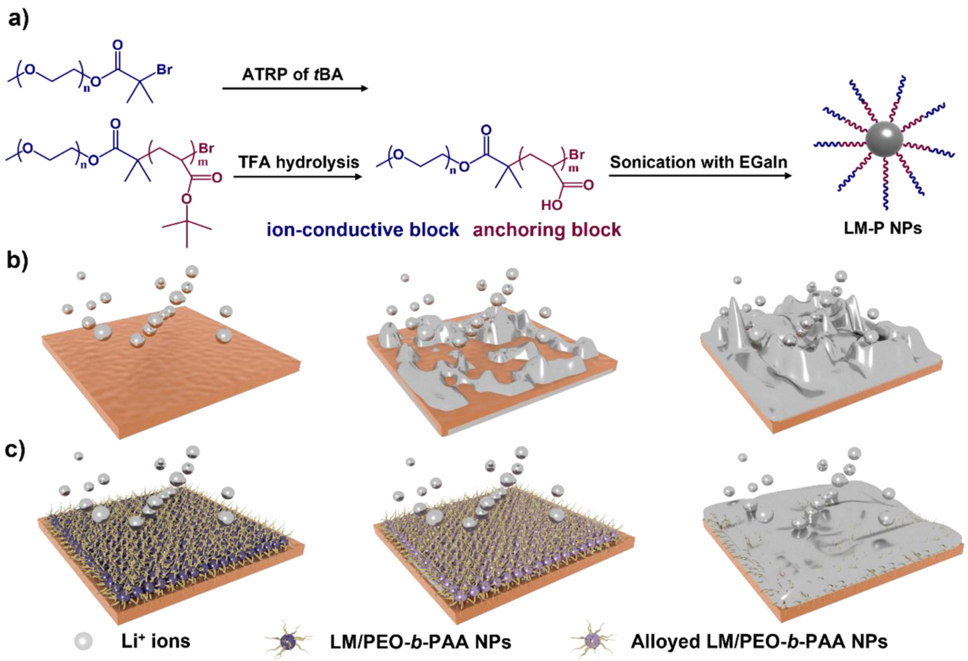

Figure 1. (a) Synthetic route to PEO_n-*b*-PAA_m block copolymer-stabilized EGaIn nanoparticles (LM-P NPs). (b) Schematic illustration of Li nucleation and deposition behaviors on (b) bare Cu (top) and (c) LM-P@Cu (bottom).

90−150 mAh/cm^2 areal capacity) is often used as a reservoir to replenish the Li loss during cycling, which can severely decrease the energy density of the batteries.[23] In order to meet practical performance targets, thinner Li metal anodes (≤30 μm) are desired; however, with thin Li metal, the suppression of dendrites and formation of "dead" Li become even more critical when targeting a full Li utilization.[4,42] Therefore, recent studies have focused on engineering current collectors to regulate the initial Li nucleation behavior, which can then significantly influence the growth and morphology of plated Li.[43−45] Polymers with lithiophilic polar groups can homogenize the Li ion concentration near the anode and promote uniform Li deposition.[46] For example, poly(*N*-isopropylacrylamide) brushes can act as channels for Li transport and enable smooth growth of Li, thanks to the interactions of Li ions with −NH and −C=O groups.[47] Moreover, it was demonstrated that Li alloys, e.g., Li−Zn, Li−Ga, Li−Sn, Li−Ag, and Li−In, are promising current collectors, owing to their fast Li ion transport and diffusion properties.[48−53] Given these facts, the creation of hybrid systems that integrate the advantages of polymers and alloys holds promise for overcoming the challenge of engineering stable Li metal anodes. Some precedent exists for hybrid structural designs that regulate Li nucleation behavior;[54] however, sophisticated and demanding preparation processes,[55] high cost,[56] and poorly controlled polymerizations[57] are important limitations for large-scale production. Further development of such polymer-alloy fabrication is needed to enable practical use of Li metal batteries.

Eutectic gallium indium (EGaIn) alloy (75% Ga and 25% In by weight) is liquid at room temperature (m.p. 15.5 °C), and it has shown great promise for electronic, robotic, and biomedical applications over the past decade, due to its flexibility, good shape transformability, high electrical and thermal conductivity, and self-healing properties.[58−61] Moreover, polymers can stabilize EGaIn to form micro/nanosized particle brushes with uniform shape, narrow size distribution, and isotropic distribution of properties.[62] The liquid characteristics of the functionalized particle brushes offer a promising fabrication method that is feasible and scalable. This work builds on the understanding developed through incorporating eutectic alloys in lithium metal batteries.[63−67]

The underlying mechanism of Li nucleation and growth on Li metal anodes typically includes (i) the initial binding of Li ions to adsorption sites at the electrode/electrolyte interface and (ii) the diffusion of Li ions through the SEI layer to reach the bulk electrode. Considering this mechanism, herein, we propose the use of polymer-stabilized liquid metal nanoparticles (LM-P NPs) of EGaIn as a coating layer on copper foil current collectors, to achieve uniform Li nucleation and deposition. Poly(ethylene oxide)-*block*-poly(acrylic acid) (PEO-*b*-PAA) was prepared by atom transfer radical polymerization (ATRP) and postpolymerization modification. It should be noted that the selection of polymers may have a significant impact on the CE due to the possible interaction of Li with the polymers,[68] while in this study, PEO chains were employed to ensure suitable ionic conductivity for Li ion transport and PAA chains provided interaction sites with EGaIn. The obtained LM-P NPs were coated on Cu foils with controlled thickness (600 nm), by a facile and scalable spray coating method. The overall structural and compositional merits of LM-P coating can endow two-dimensional growth of Li, instead of a dendritic Li morphology (Figure 1b,c), resulting in low nucleation overpotentials and regulated Li stripping/plating in symmetric cells and full cells. This result can be attributed to (i) PEO-*b*-PAA copolymers acting as lithiophilic binding sites for Li ions, guiding the homogeneous Li distribution on the substrate surface; (ii) EGaIn NPs reducing the diffusion barrier of Li via the alloying process, leading to fast Li transport and low nucleation overpotential; (iii) the infusion of Li into EGaIn resulting in a "surface" growth pattern, thus suppressing the formation of Li dendrites and "dead" Li; and (iv) the particle brush architecture of LM-P

https://doi.org/10.1021/acsaem.1c04106
ACS Appl. Energy Mater. 2022, 5, 3615−3625

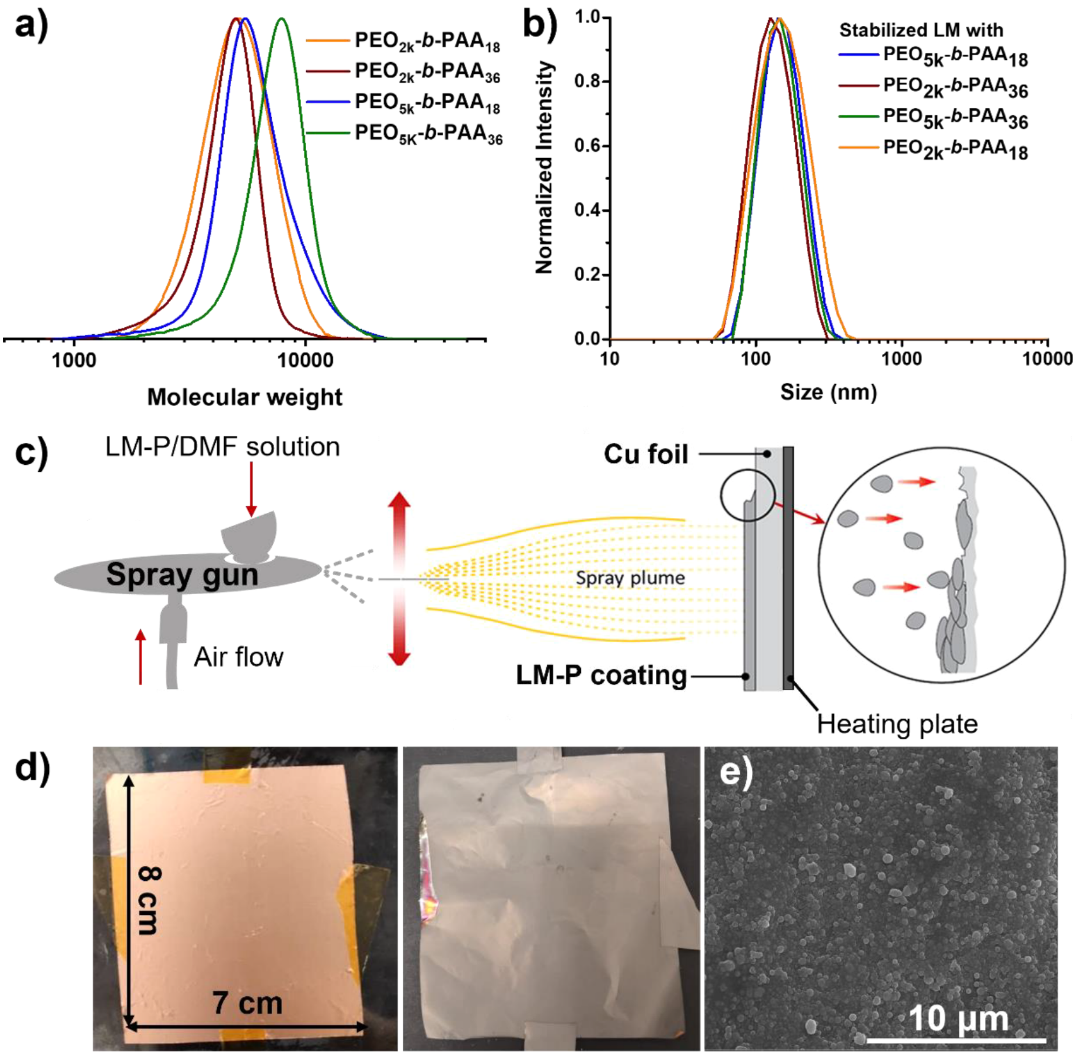

Figure 2. (a) GPC traces of different molecular weight PEO-*b*-PAA polymers. (b) DLS traces of LM-P NPs. (c) Schematic illustration of the spray coating process of LM-P NPs onto a Cu foil. (d) Photographs of the Cu foil before (left) and after spray coating with the LM-P NP suspension (right). (e) SEM image of the LM-P coating on Cu. Scale bar: 10 μm.

NPs providing sufficient connection between the polymers and LM NPs to ensure regulated pathways for Li transport.

RESULTS AND DISCUSSION

Preparation and Characterization of LM-P NPs. The fabrication of LM-P NPs started with the synthesis of PEO-*b*-PAA block copolymers through ATRP,[69−72] which provided copolymers with a well-controlled molecular weight (MW), narrow MW distribution, and precise architecture (Figure 1a). α-Bromoisobutyryl bromide was used for the modification of poly(ethylene glycol)methyl ether to install C−Br chain ends, which served as ATRP initiating sites. After obtaining the PEO−Br macroinitiator, ATRP of *tert*-butyl acrylate (*t*BA) was performed via the activator regenerated by electron transfer method.[73−76] A series of PEO$_n$-*b*-P*t*BA$_m$ copolymers was obtained with different lengths of each block, with "*n*" indicating the number-average MW of PEO (M_n = 2000 or 5000) and "*m*" representing the average degree of polymerization of P*t*BA ("*m*" = 18 or 36). Polymer MWs were measured by gel permeation chromatography (GPC). As shown in Figure 1a and Table S1, samples of PEO$_{2k}$-*b*-P*t*BA$_{18}$, PEO$_{2k}$-*b*-P*t*BA$_{36}$, PEO$_{5k}$-*b*-P*t*BA$_{18}$, and PEO$_{5k}$-*b*-P*t*BA$_{36}$ had M_n values of 4300, 4700, 5500, and 5700, respectively. Copolymer dispersities were all <1.16, indicative of well-controlled polymerizations. To graft polymers onto EGaIn, trifluoroacetic acid (TFA) was used for the hydrolysis of the P*t*BA blocks, forming carboxylic acid functional groups that are capable of etching the surface gallium oxide layer of EGaIn. After hydrolysis, PEO$_n$-*b*-PAA$_m$ copolymers were obtained and dissolved in dimethylformamide (DMF), resulting in transparent yellowish solutions, to which EGaIn liquid metal was added. The resulting mixtures were ultrasonicated for 1 h in an ice bath. LM-P NP suspensions in DMF, which appeared as light gray slurries (Figure S1), were obtained upon sonication. The LM-P NPs maintained excellent colloidal stability for months since polymers acted as effective surfactants; however, limited sediments were observed, presumably caused by the high specific density of EGaIn. In contrast, LM NPs without polymer stabilization experienced phase separation and completely agglomerated at the bottom of the vial within less than 1 h. The suspension of LM-P NPs was analyzed using dynamic light scattering (DLS) to measure the hydrodynamic size of the LM-P NPs. As shown in Figure 2b, samples with composition LM/PEO$_{2k}$-*b*-PAA$_{18}$, LM/PEO$_{2k}$-*b*-PAA$_{36}$, LM/PEO$_{5k}$-*b*-PAA$_{18}$, and LM/PEO$_{5k}$-*b*-PAA$_{36}$ had average sizes of

https://doi.org/10.1021/acsaem.1c04106
ACS Appl. Energy Mater. 2022, 5, 3615−3625

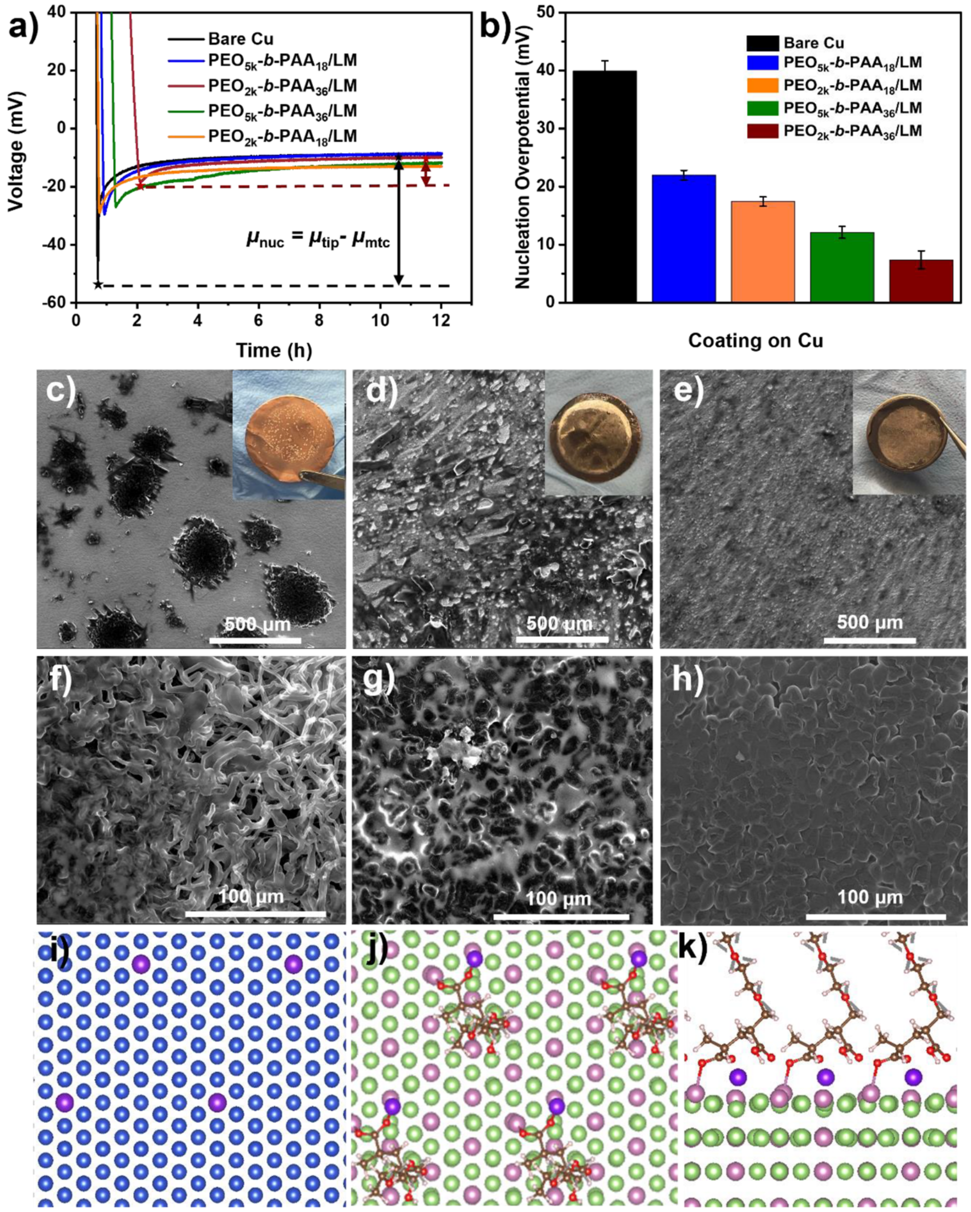

Figure 3. (a) Galvanostatic Li electrodeposition voltage profiles measured in Cu|Li and LM-P@Cu|Li cells with LM-P NP coatings with different compositions, at 0.05 mA cm^{-2}. (b) Li nucleation overpotentials calculated from the measurements in (a). The reported values are average values of three repeated measurements made for each conditioned cell. (c−e) SEM images of 2 μm Li deposition at 0.05 mA cm^{-2} on bare Cu, LM@Cu and LM-P@Cu (with PEO$_{2k}$-*b*-PAA$_{36}$) substrates, respectively. Insets: Images of 2 μm Li deposition on the three substrates. (f−h) SEM images of 30 μm Li deposition at 0.05 mA cm^{-2} and then 0.5 mA cm^{-2} on bare Cu, LM@Cu, and LM-P@Cu (with PEO$_{2k}$-*b*-PAA$_{36}$) substrates, respectively. (i and j) Top-view simulated binding environments of Li atoms on bare Cu and LM-P@Cu, respectively. (k) Side-view simulated binding environments of Li atoms on LM-P@Cu. Lithium atoms interact with polymer molecules as well as pristine Ga−In substrates. Blue: Cu, purple: Li, pink: In, green: Ga, brown: C, red: O, white: H.

139.0, 123.7, 142.2, and 139.9 nm, respectively. The hydrodynamic size of the LM-P NPs increased with the increasing length of the PEO block. However, longer PAA chains resulted in smaller size of the LM-P NPs, due to the higher concentration of interacting sites, which strengthened the anchoring effect onto EGaIn. Thus, the MWs of the PEO and PAA blocks can be used to manipulate the size of LM-P NPs. Transmission electron microscopy images showed that LM-P NPs were uniformly distributed with little noticeable aggregations due to the modification of PEO-*b*-PAA copolymers, where the thickness of the polymer layers was ~10 nm. In sharp contrast, LM NPs without polymers showed high extent of aggregation and irregular shape of the particles (Figure S2).

The structure of the LM-P NPs was examined by X-ray photoelectron spectroscopy (Figure S3). The two strong peaks located at 451.0 and 443.3 eV were attributed to In 3d$_{3/2}$ and In 3d$_{5/2}$, respectively. Four peaks in the high-resolution spectrum of the Ga 3d region were observed and assigned to O 2s, Ga−O, Ga, and In 4d, in agreement with other reports.[77] The C 1s signal (O−C) at about 287.2 eV and O 1s signals (C−O; C=O) at 531.4, and 532.8 eV were attributed to the copolymers. To further prove the attachment of polymer chains onto EGaIn, thermogravimetry was performed (Figure S4). In comparison with pure copolymers and with LM NPs without copolymers, the weight loss observed for the LM-P NPs in the temperature range 120−400 °C supports the presence of copolymers grafted onto EGaIn.

Fabrication of the LM-P Coating on Cu and Li Nucleation Study. LM-P NPs were coated on Cu foil by a facile and scalable spray coating method (Figure 2c). A precut Cu foil with a surface area of 7 × 8 cm was taped onto a vertical heating plate, which was then heated to 150 °C. The LM-P NP suspension in DMF (concentration 11 mg mL^{-1}) was loaded into the spray gun. Using a constant airflow, the LM-P NP suspension was uniformly painted onto the Cu foil and DMF immediately evaporated upon contact with the heated Cu surface. The obtained LM-P NP-coated Cu (LM-P@Cu) appeared shiny and light gray colored, as shown in Figure 2d. Scanning electron microscopy (SEM) and energy-dispersive X-ray spectroscopy (EDS) were employed to examine the surface morphology and elemental composition of LM-P@Cu. Regular and spherical LM-P NPs were uniformly distributed on the surface of Cu (Figures 2e and S5b). In contrast, an LM NP coating on Cu lacking the copolymer layer (denoted as LM@Cu) showed aggregated particles and inhomogeneous coverage of the Cu surface (Figure S5c). These observations further substantiated the critical role of PEO-*b*-PAA copolymers in stabilizing the LM NPs, thus enhancing the homogeneity of the coating. Cross-section SEM was used to study the thickness of the LM-P NP coating, which was about 600 nm (Figure S5a). LM-P@Cu examined by SEM after 30 cycles in a Cu|Li cell after full Li stripping confirmed that the original spherical particle morphology of LM-P NPs was well-maintained but with a flatten surface and condensed structure due to the repeated cycling (Figure S5d). EDS showed that C and O atoms in the copolymer chains and Ga and In in the EGaIn NPs were evenly coated on the Cu surface, in accordance with the top-view SEM (Figure S6). To investigate the reversible alloying process between Li and LM-P NPs, the cyclic voltammetry test was performed for the Li|LM-P@Cu cell at a scan rate of 0.01 mV s^{-1} in a voltage range of 0−1.5 V (versus Li^+/Li) (Figure S7). The result corresponded to previous reports on the alloying of Li−Ga and Li−In.[60,65,78]

Contact angle measurements revealed the wetting behavior of an ether-based liquid electrolyte on the different Cu substrates (Figure S8). The smallest contact angle (5.3°) was obtained for LM-P@Cu, indicating a low surface tension and good wetting. In contrast, larger contact angles were observed for bare Cu (44.5°) and LM@Cu (27°). As shown in Figure S9, LM-P@Cu was further soaked in the liquid electrolyte for 2 weeks; however, no dissolution of the LM-P coating was observed, confirming the stability and good adhesion of the coating layer. Asymmetric Li cells (LM-P@Cu|Li and bare Cu|Li) were assembled and tested at a fixed current density of 0.05 mA cm^{-2} for 12 h, to study the Li nucleation behavior on the various substrates. The nucleation overpotentials (μ_{nuc}) were calculated by considering the differences between a tip potential (μ_{tip}) and a mass-transfer controlled potential (μ_{mtc}). The lower Li nucleation overpotentials of the various LM-P@Cu substrates compared to bare Cu (Figure 3a,b) indicate that the coatings promoted stable Li nucleation and uniform growth of the Li nuclei through and above the coating. In contrast, the intrinsic roughness and defects on the bare Cu surface and its lithiophobic nature led to random Li nucleation and uneven growth of Li nuclei, which eventually resulted in the formation of dendritic Li and the measurement of a larger nucleation overpotential (39.9 mV). The effect of different compositions of the LM-P NP coatings on the Li nucleation process was also explored. As shown in Figure 3a,b, the lowest nucleation overpotential (7.4 mV) was observed with PEO_{2k}-*b*-PAA_{36} (9 wt %)-stabilized LM-P NPs, suggesting that LM-P NPs with a relatively small size can contribute to more uniform Li nucleation. Based on the Li nucleation performance, LM-P NPs with the copolymer PEO_{2k}-*b*-PAA_{36} was selected for further electrochemical characterizations. The effect of coating thickness on Li nucleation was investigated (Figure S10). Thinner coatings (∼120 and ∼240 nm) manifested higher nucleation overpotentials, likely because of uneven distribution of the coating layer during the spray coating process when the coating layer was too thin. It should be noted that because of the inhomogeneous and aggregated nature of the LM NP coating without copolymers, it was not possible to obtain an average and stable nucleation overpotential for LM@Cu (Figure S10c).

After selecting the most appealing composition of the LM-P NP coating on Cu, the nucleation and deposition of Li were examined by SEM (Figure 3c−h). Both 2μm Li and 30 μm Li were electrodeposited on bare Cu, LM@Cu, and LM-P@Cu substrates, respectively, in Cu|Li cells at 0.05 mA cm^{-2}. The 2 μm Li deposition on bare Cu showed irregularly shaped, mossy Li nuclei and rather random nucleation spots (Figure 3c). Images of 2 and 30 μm Li deposition on the three substrates are shown in Figure 3c−e insets and S11. In comparison, LM@Cu was able to alloy with Li, resulting in a smoother surface but with gyroid-like morphology (Figure 3d). Finally, the LM-P@Cu substrate promoted more uniform nucleation of Li, benefiting from uniform copolymer binding sites (Figure 3e). The initial nucleation behavior and the resulting interphase layer influenced the deposition process, as shown in Figure 3f−h. The deposited 30 μm Li on bare Cu exhibited a dendritic and porous structure, while for LM@Cu and LM-P@Cu, the Li deposits were densified and exhibited a two-dimensional growth. However, partial aggregation was observed on the LM@Cu substrate, due to the relatively inhomogeneous deposition in the absence of the functional groups of the copolymers. In addition, cross-section SEM showed a large gap between the deposited Li and the bare Cu surface due to the poor adhesion. In contrast, LM@Cu provided improved adhesion, and LM-P@Cu had the smallest interfacial gap, benefiting from the strongest adhesion with deposited Li (Figure S12).

To explain the variation of nucleation overpotential and deposition morphology over different surfaces, density functional theory (DFT) calculations were performed using the real space projector-augmented wave method implemented in the GPAW code.[79] Lithium adsorption energies were calculated for the corresponding current collector surfaces. The Cu(111) surface was selected for bare Cu due to its low surface energy (Table S3). Figure 3i−k shows simplified binding structures of Li with a bare Cu surface and LM-P NP coating. An adsorption energy of 0.77 eV was obtained for lithium atoms on bare Cu. In the LM-P@Cu scenario, PEO_{2k}-*b*-PAA_{36} copolymers were coated on the EGaIn surface as initial adsorption sites for lithium (Figure 3j). To simplify the calculation process, PEO-*b*-PAA molecules with two repeat units for each block were used. The modified surface provided a lithium adsorption energy of 1.26 eV, indicating a stronger interaction between lithium atoms and the LM-P NP coating. Therefore, there is likely a nucleation overpotential decrease when coating the

https://doi.org/10.1021/acsaem.1c04106
ACS Appl. Energy Mater. 2022, 5, 3615−3625

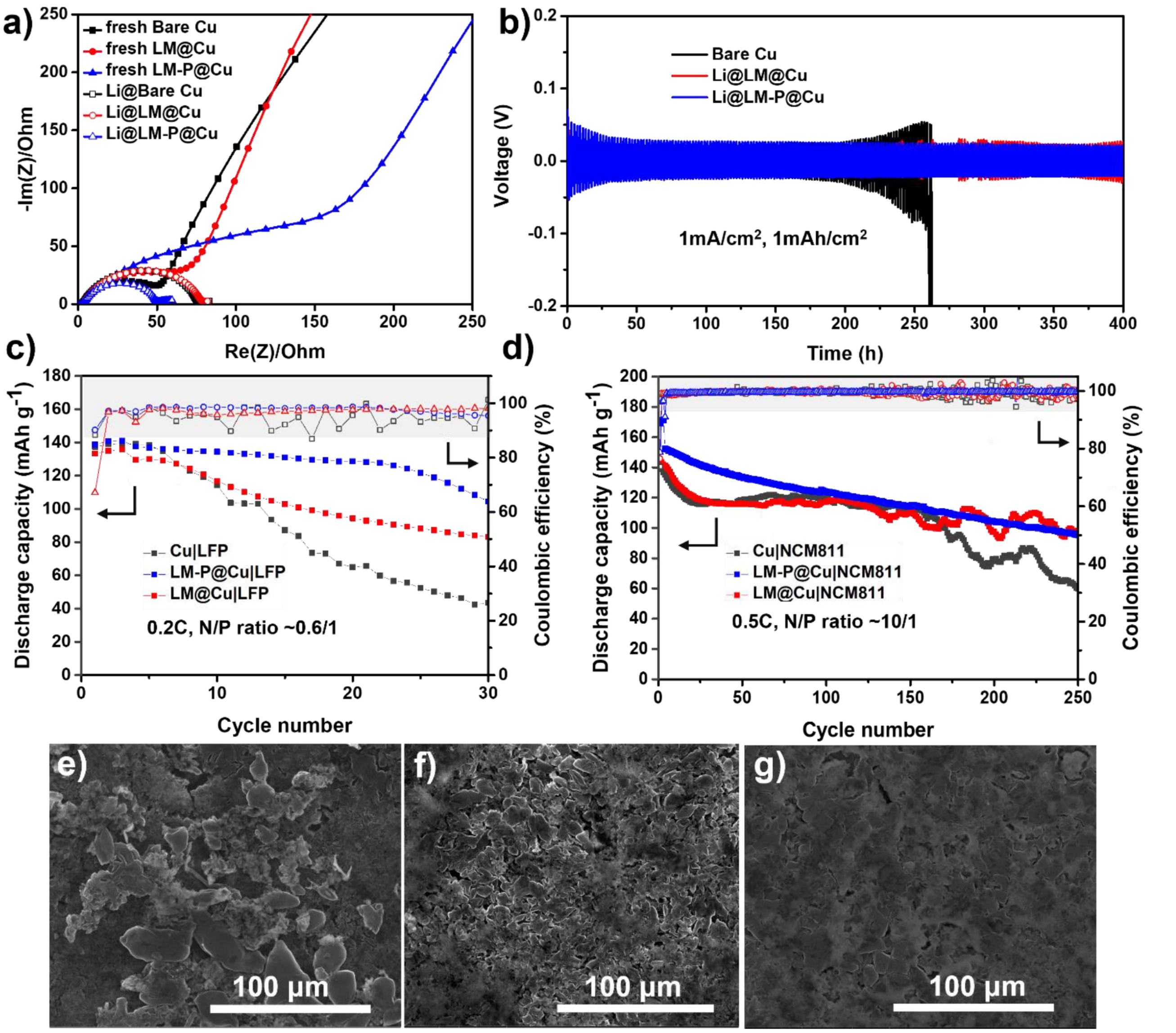

Figure 4. (a) Li|Cu cell resistance measured by EIS before and after 30 μm Li deposition on bare Cu (black), LM@Cu (red), and LM-P@Cu (blue). (b) Galvanostatic cycling of Cu|Li cells with bare Cu (black), LM@Cu (red), and LM-P@Cu (blue) electrodes at 1 mA cm^{-2} and 1 mAh cm^{-2}. (c) Capacity retention vs cycle number of Li|LFP cells with an N/P ratio of ~0.6/1 at 0.2C, with Li predeposited on bare Cu (black), LM@Cu (red), and LM-P@Cu (blue) substrates. The first three cycles are formation cycles at 0.1C. (d) Capacity retention vs cycle number of Li|NCM811 cells with an N/P ratio of ~ 10/1 at 0.5C, with Li predeposited on bare Cu (black), LM@Cu (red), and LM-P@Cu (blue) substrates. (e−g) SEM images of the cycled lithium anode on bare Cu, LM@Cu, and LM-P@Cu, respectively, from disassembled Li|NCM811 cells after 250 cycles.

LM-P NP layer on Cu. However, analyzing the growth of the layer will require understanding lithium adsorption at high coverage, which is beyond the scope of the current study. More details on calculator settings and surface structures can be seen in the SI.

Electrochemical Cycling Performance. A series of electrochemical tests of the three anodes was conducted. Electrochemical impedance spectra (EIS) of Li|Cu cells using bare Cu, LM@Cu, and LM-P@Cu before and after the 30 μm Li deposition were compared to determine the interfacial impedance (Figure 4a). The bare Cu had the smallest interfacial impedance (50.48 ohm) before Li deposition; however, it greatly increased after Li deposition (79.14 ohm), indicating that the uneven deposition of Li on bare Cu leads to an irregular and thick SEI layer that enhances the interfacial resistance. Also, LM@Cu showed a larger impedance than bare Cu before Li deposition and an increased resistance after Li deposition. In contrast, LM-P@Cu had the largest interfacial impedance (155.9 ohm) before Li deposition, likely because of the dielectric nature of organic polymers; however, the resistance significantly decreased to 50.20 ohm after Li deposition. This large decrease was attributed to the formation of a smooth SEI and homogeneous Li deposits. In Figure S13 and Table S2, the stability of Li stripping/plating was studied in Cu|Li cells at 1 mA/cm^2, where LM-P@Cu exhibited the highest CE of 99.36%, while the bare Cu|Li and LM@Cu|Li cells had Coulombic efficiencies of 98.87 and 99.05%, respectively. Asymmetric Li|Li@Cu cells were assembled using the three Cu substrates and an ether-based liquid electrolyte, and their long-term cycling stability was tested at a current density of 1 mA cm^{-2} and areal capacity of 1 mAh cm^{-2} (Figure 4b). The Li|Li@Cu cell (i.e., with bare Cu)

https://doi.org/10.1021/acsaem.1c04106
ACS Appl. Energy Mater. 2022, 5, 3615−3625

started to polarize after 200 h, due to the depletion of deposited Li on the Cu side. Conversely, the Li|Li@LM@Cu and Li|Li@LM-P@Cu cells exhibited good stability for over 400 h of cycling. Nevertheless, the Li@LM@Cu electrode experienced voltage fluctuations, which were attributed to the rather inhomogeneous LM coating on Cu. A high current density of 5 mA/cm^2 and areal capacity of 3 mAh/cm^2 were further applied to the Li|Li@LM-P@Cu cells (Figure S14), the cycling performance of which showed an initial stabilization process due to the Li alloy formation and possible interaction of Li with residual PAA blocks of the polymers. After the interfacial layer was densified, the overpotential of the cell significantly decreased and lasted for more than 400 h.

To test the stability of Li@LM-P@Cu under practical and commercially relevant conditions, a low negative/positive electrode capacity (N/P) ratio was designed in this study. Then, 1 μm Li was deposited on the three Cu substrates and then paired with the $LiFePO_4$ (LFP) cathode and an ether-based electrolyte. LFP was chosen due to its structural and thermal stability compared to Ni-rich cathodes. A low N/P ratio ∼ 0.6 was designed, and the resulting Li@LM-P@Cu|LFP cell delivered a significantly higher capacity than Li@LM@Cu and Li@Cu cells, the capacity of which dropped abruptly after 10 cycles (Figure 4c). Then, 30 μm Li anodes paired with an $LiNi_{0.8}Co_{0.1}Mn_{0.1}O_2$ (NCM811) cathode with an N/P ratio of 10 were examined in a carbonate-based liquid electrolyte to verify the capability of LM-P stabilizing the Li anode with different cathode chemistries. The rate capability of the full cells was tested at variable C-rates from 0.2 to 5C between 2.9 and 4.3 V (Figure S15), and the corresponding voltage−capacity curves are presented in Figure S16. The cell containing the Li@LM-P@Cu anode showed a higher specific capacity than Li@LM@Cu and Li@Cu cells at all rates: 0.1C (152.9 mAh/g), 0.2C (124.8 mAh/g), 0.5C (99.2 mAh/g), 1C (69.7 mAh/g), and 2C (21.8 mAh/g). The long-term cycling performance of the full cells was also studied (Figure 4d). The full cell with an Li@LM-P@Cu anode exhibited good capacity retention, preserving a capacity of 97.4 mAh/g after 250 cycles, with an average CE of 99.55%. In contrast, Li@LM@Cu|NCM811 and Li@Cu|NCM811 cells showed a fast capacity decay within the first 30 cycles and large fluctuation of CE and capacity after 100 cycles, indicative of severe surface reconstruction processes that could consume Li and lead to uneven surfaces and formation of "dead" Li. The surface morphology of the cycled anodes was analyzed by SEM (Figure 4e−g). The surface of Li deposited on bare Cu showed large Li islands after 200 cycles. In contrast, Li@LM@Cu showed smaller "pulverized" particles, while the Li@LM-P@Cu electrode showed the flattest and smoothest surface. The charge and discharge curves of the three full cells are presented in Figure S17, further revealing the tendency and rate of the capacity decay. The cell using bare Cu had the fastest capacity decay and large polarization, while the cell with the LM coating on Cu had a much lower capacity decay rate. Finally, the cell with LM-P@Cu had the smallest polarization and capacity decay.

■ CONCLUSIONS

In summary, the combination of functional polymers and liquid metal alloys provides a new avenue to regulate Li stripping/plating. The PEO_n-*b*-PAA_m copolymers can effectively stabilize EGaIn NPs by anchoring onto the surface, providing nanosized particle brushes with uniform, lithiophilic binding sites. The formation of Li−Ga and Li−In alloy during the insertion of Li provides ultralow nucleation overpotential and fast transport and diffusion, resulting in a two-dimensional growth of Li with a smooth and flat surface. Moreover, the Li nucleation behavior was analyzed systematically by tuning the composition of the polymers, providing new perspectives for the rational design of functional polymers and synergistic alloys in the context of homogenizing Li nucleation and deposition. Remarkable rate capability and stable cycling performance of Li@LM-P@Cu anodes in Li|NCM811 cells for more than 250 cycles with a high average CE (99.55%) were achieved, which demonstrated the potential and promises of advancing the commercialization of Li metal batteries as a proof-of-concept. Li@LM-P@Cu enabled higher specific discharge capacities and improved capacity retention compared to Li@Cu and Li@LM@Cu anodes in Li|LFP cells with a low N/P ratio of ∼ 0.6. DFT simulations were carried out to understand the Li binding and adsorption properties by determining the binding energy between the coated Cu substrate and Li. Finally, the facile fabrication method of the LM-P coating on Cu is compatible with large-scale production and sheds light on the future development of anode-free systems by current collector engineering.

■ EXPERIMENTAL SECTION

Materials. *tert*-Butyl acrylate (*t*BA, Sigma-Aldrich, >99%) was purified by passing through a basic alumina column before use. Poly(ethylene glycol) methyl ether (PEO_{5k}, M_n = 5000 g/mol, Aldrich, and PEO_{2k}, M_n = 2000 g/mol, Aldrich), copper bromide ($CuBr_2$, Aldrich, 99%), triethylamine (TEA, Alfa Aesar, 99%), tin(II) 2-ethylhexanoate ($Sn(EH)_2$, 95%, Aldrich), tris(2-dimethylaminoethyl)amine (Me_6TREN, Alfa Aesar, 99%), α-bromoisobutyryl bromide (98%, Aldrich), indium (Alfa, 99.999%), gallium (Alfa, 99.99%), *N*,*N*-dimethylformamide (DMF, VWR, 99%), diethyl ether (Fisher, 99%), hydrochloric acid (HCl, Fisher, 36.5−38.0%), and trifluoroacetic acid (TFA, 99%, Aldrich) were used as received.

Nuclear Magnetic Resonance Spectroscopy (NMR). ^{1}H NMR spectroscopy measurements were performed with a Bruker Advance 300 MHz spectrometer using $CDCl_3$ as the solvent.

Gel Permeation Chromatography (GPC). Number-average MWs (M_n) and molecular weight distributions of PEO_n-*b*-PAA_m polymers were determined by GPC. The GPC system used a Waters 515 HPLC pump and a Waters 2414 refractive index detector using Waters columns (Styrogel 10^2, 10^3, and 10^5 Å) with 10 mM LiBr-containing DMF as the eluent at a flow rate of 1 mL/min at 50 °C using linear poly(ethylene oxide) (PEO)-based calibrations. Toluene was used as the internal standard for the system.

Dynamic Light Scattering (DLS). DLS using a Malvern Zetasizer Nano ZS was employed to determine volume-weighted average hydrodynamic diameters and distribution of LM NPs. The particle brushes were suspended in filtered DMF (4.5 μm PTFE filter) at low concentrations.

Transmission Electron Microscopy (TEM). TEM was performed using a 200 kV FEI Tecnai F20 Super-Twin transmission electron microscope equipped with a Gatan Orius CCD camera, recorded on the Gatan Microscopy Suite software.

Scanning Electron Microscope (SEM). SEM was performed for surface morphology investigation and conducted with a Quanta 600 FEG instrument. An Oxford INCA EDS System full analytical and XMAX 80mm SDD EDX detector was used for energy-dispersive spectroscopy analysis.

Thermogravimetric Analysis (TGA). TGA with a TA Instruments 2950 was used to measure the fraction of YSZ in the hybrids. The data were analyzed with TA Universal Analysis. The heating procedure involved four steps: (1) temperature jump to 120 °C; (2) hold at 120 °C for 10 min; (3) ramp up at a rate of 20 °C/min to 800

https://doi.org/10.1021/acsaem.1c04106
ACS Appl. Energy Mater. 2022, 5, 3615−3625

°C; and (4) hold for 2 min. The organic content of the samples was normalized to the weight loss between 120 and 800 °C.

X-Ray Photoelectron Spectroscopy (XPS). The XPS spectra were collected using a ThermoFisher ESCALAB 250 Xi instrument with a 650 μm acquisition spot size, and each plot represents the average of at least 10 scans. A flood gun was used during data collection, and each spectrum was referenced to the adventitious carbon peak at 284.8 eV. The spectra were fit using Thermo Avantage software. For fitting the high-resolution Ga 3d spectra, the spin−orbit components were simplified to one peak because of the small energy splitting and overlapping Ga−O, Ga, and In 4d peaks.

Electrochemical Testing. Electrochemical characterization was carried out using CR2032-type coin cells. To evaluate the electrochemical nucleation and deposition behavior, LM-P@Cu, LM@Cu, and bare Cu were used as the target current collectors, and Li foil was used as the lithium reservoir. Lithium bis(trifluoromethanesulfonyl)imide (LiTFSI) (1 M) in a mixed solution of 1,3-dioxolane (DOL) and dimethoxyethane (DME) (1:1 v/v) with 2 wt % lithium nitrate was used as the electrolyte. Then, 6 mAh cm^{-2} of Li was plated onto LM-P@Cu, LM@Cu, and bare Cu at a current density of 0.25 mA cm^{-2} to form the Li@LM-P@Cu, Li@LM@Cu, and Li@Cu electrodes. Symmetric cells were assembled using Li@LM-P@Cu, Li@LM@Cu, and Li@Cu electrodes to measure the long-term electrochemical behavior of Li plating/stripping at 1 mA cm^{-2} and 1 mAh cm^{-2}. For Li|NCM811 cells, the cathode contains 80 wt % of commercial NCM811 powder, 10 wt % of Super-p, and 10 wt % of polyvinylidene difluoride binder using *N*-methyl-2-pyrrolidone as the solvent, and the well-mixed slurry was cast onto Al foil (mass loading ∼3 mg/cm^2). $LiPF_6$ (1.0 M) in ethylene carbonate and ethyl methyl carbonate (v/v = 1:1) with 5 wt % fluroethylene carbonate was used as the electrolyte to meet the voltage operating window. For Li|LFP cells, the cathode contains 80 wt % of commercial LFP powder, 10 wt % of Super-p, and 10 wt % of polyvinylidene difluoride binder using *N*-methyl-2-pyrrolidone as the solvent, and the well-mixed slurry was cast onto Al foil (mass loading 2.5 mg/cm^2). LiTFSI in a solution mixture of DOL and DME (1:1 v/v) with 2 wt % lithium nitrate was used as the electrolyte. For all the battery assembly, 50 μL of electrolyte was used in each coin cell to standardize the testing. All the cells were assembled in a glove box with water/oxygen content lower than 0.5 ppm and were tested at room temperature. For measurement of CE, a fixed amount of charge (Q_T = 6 mAh/cm^2) was deposited onto the working electrode and then a smaller portion of the charge (Q_c = 1 mAh/cm^2) was used to cycle Li between working and counter electrodes for *n* cycles. The final stripping charge (Q_S) was stripped away up to 0.5 V. A current density of 1 mA/cm^2 was applied to the whole process. The average CE over *n* cycles can be calculated using the formula

$$CE_{arg} = \frac{nQ_C + Q_S}{nQ_C + Q_T}$$

Synthesis of PEO-*b*-P*t*BA Block Copolymers. PEO_{2k}-Br (1.0 g, 0.75 mmol), *t*BA (2.93 mL, 30 mmol), $CuBr_2$ (2.5 mg, 11.3 μmol), Me_6TREN (12 μL, 67.5 μmol), and anisole (8.77 mL, 75 vol %) were mixed in a Schlenk flask. The flask was sealed and degassed by N_2 bubbling for 15 min to remove oxygen. Then, 0.1 mL of degassed $Sn(EH)_2$ was injected into the reaction mixture. The flask was then transferred to an oil bath set at 60 °C to start the reaction. Samples were withdrawn from the reaction by degassed syringes at timed intervals, and the conversion was monitored with ^{1}H NMR. At the desired conversion, the reaction was quenched by addition of THF and exposure to air. The mixture was passed through a flash column filled with neutral alumina to remove the catalyst. The PEO-*b*-P*t*BA polymers were isolated by precipitation in cold ethyl ether. Then, 1 g of PEO-*b*-P*t*BA block copolymer was dissolved in 10 mL of DCM. While the solution was stirred vigorously, 2.0 mL of TFA was added slowly to the reaction mixture and then stirred at room temperature for 48 h. PEO-*b*-PAA was obtained after removal of the solvent and residual acid under vacuum.

Preparation of LM-P NPs. To make the eutectic gallium indium alloy consisting of 75.5 wt % Ga and 24.5 wt % In, 50.0 g of as-received gallium was first melted at 50 °C in a 50 mL beaker. The melted Ga was then added to 16.2 g of indium shots and stirred at 190 °C for 2 h. The liquid EGaIn alloy was brought back to room temperature on a hot plate and stored in a closed container. Then, 200 mg of the obtained EGaIn was added into a 20 mL vial containing 10 mL of DMF copolymer solution. The mixture was sonicated with a probe (Sonics VCX500, 500 W, 25% amplitude) in an ice bath for 1 h. After sonication, the gray suspension was diluted and used for DLS analysis and the spray coating process directly.

Spray Coating of LM-P NPs on Cu Foil. The LM-P NPs/DMF suspension was added to a spray gun (Master, Airbrush, G22). With a constant airflow, the liquid spray was uniformly painted on a Cu foil that was preheated to 150 °C. The coating layer was immediately formed upon contact with the Cu foil. The as-obtained coated Cu foil was then peeled off from the heating plate. After cooling down to room temperature, the coated Cu foil is ready to use as the modified current collector in coin cells.

Computations. Self-consistent DFT calculations were performed using the real space projector-augmented wave method implemented in the GPAW code.[79] The Perdew−Burke−Ernzerhof exchange−correlation functional[80] was used for all DFT calculations due to its accuracy for conducting this type of task.[47,55,81] All geometry optimizations were done with a force criterion of 0.05 eV/Å. A Monkhorst-Pack Brillouin-zone sampling was used. The density of *k*-points (for the Brillouin-zone sampling) and the number of grid points (for finite-difference mode of wave function expansion) were chosen after the convergence test over bulk energies with criteria of 10 meV/atom. Bare copper and alloy surfaces were created with four layers, with two bottom layers fixed, which were found to well-converge with respect to surface energies. Periodic boundary conditions were applied to the directions in parallel to the slab. Then, 10 angstrom vacuum was added in the nonperiodic direction. Calculations for all low miller-index stoichiometric and symmetric surfaces were conducted to derive their surface energies, as shown in Table S3. The Cu(111) and $InGa_3$(111) surface has been selected for binding energy calculation owing to its low surface energies and hence stability in nature. Binding energy calculation was conducted as follows: $E_{binding}=(E_{slab} + E_{Li}) - E_{slab + Li}$, where E_{slab}, E_{Li}, and $E_{slab + Li}$ denote the free energies of the pristine substrate slab, the reference lithium atom, and the binding structure, respectively. All symmetry sites over surfaces were exhaustively tested over lithium-ion binding energies, and results of the most stable binding site are reported.

■ ASSOCIATED CONTENT

Supporting Information

The Supporting Information is available free of charge at https://pubs.acs.org/doi/10.1021/acsaem.1c04106.

Experimental section, synthesis, and characterizations of diblock copolymers, additional data of LM-P NPs, and electrochemical cycling properties of stabilized Li metal anodes in symmetric cells and full cells (PDF)

■ AUTHOR INFORMATION

Corresponding Authors

Venkatasubramanian Viswanathan − *Department of Mechanical Engineering and Scott Institute for Energy Innovation, Carnegie Mellon University, Pittsburgh, Pennsylvania 15213, United States*; Email: venkatv@andrew.cmu.edu

Jay F. Whitacre − *Department of Materials Science and Engineering and Scott Institute for Energy Innovation, Carnegie Mellon University, Pittsburgh, Pennsylvania 15213, United States*; orcid.org/0000-0002-3439-4111; Email: whitacre@andrew.cmu.edu

Krzysztof Matyjaszewski − *Department of Chemistry, Carnegie Mellon University, Pittsburgh, Pennsylvania 15213, United States*; orcid.org/0000-0003-1960-3402; Email: matyjaszewski@cmu.edu

Authors

Tong Liu − *Department of Chemistry, Carnegie Mellon University, Pittsburgh, Pennsylvania 15213, United States*

Xinsheng Wu − *Department of Materials Science and Engineering, Carnegie Mellon University, Pittsburgh, Pennsylvania 15213, United States*

Shang Zhu − *Department of Mechanical Engineering, Carnegie Mellon University, Pittsburgh, Pennsylvania 15213, United States*

Francesca Lorandi − *Department of Chemistry, Carnegie Mellon University, Pittsburgh, Pennsylvania 15213, United States*; orcid.org/0000-0001-5253-8468

Longchang Ni − *Department of Mechanical Engineering, Carnegie Mellon University, Pittsburgh, Pennsylvania 15213, United States*

Sipei Li − *Department of Chemistry, Carnegie Mellon University, Pittsburgh, Pennsylvania 15213, United States*; orcid.org/0000-0001-7659-1001

Mingkang Sun − *Department of Chemistry, Carnegie Mellon University, Pittsburgh, Pennsylvania 15213, United States*; orcid.org/0000-0003-4652-5243

Brian P. Bloom − *Department of Chemistry, University of Pittsburgh, Pittsburgh, Pennsylvania 15260, United States*; orcid.org/0000-0001-9581-9710

David H. Waldeck − *Department of Chemistry, University of Pittsburgh, Pittsburgh, Pennsylvania 15260, United States*; orcid.org/0000-0003-2982-0929

Complete contact information is available at: https://pubs.acs.org/10.1021/acsaem.1c04106

Notes

The authors declare no competing financial interest.

■ ACKNOWLEDGMENTS

The authors gratefully acknowledge financial support from NSF (DMR 1501324 and 2202747) and Materials Characterization Facility at Carnegie Mellon University (grant MCF-677785). D.H.W. and B.B. acknowledge support from the US DOE Grant No. ER46430. Additional support was provided by the Scott Institute for Energy Innovation at Carnegie Mellon University. We thank Dr. Qiangbing Wei for the useful discussions.

■ REFERENCES

(1) Tarascon, J. M.; Armand, M. Issues and challenges facing rechargeable lithium batteries. *Nature* **2001**, *414*, 359−367.

(2) Lin, D.; Liu, Y.; Cui, Y. Reviving the lithium metal anode for high-energy batteries. *Nat. Nanotechnol.* **2017**, *12*, 194−206.

(3) Xu, W.; Wang, J.; Ding, F.; Chen, X.; Nasybulin, E.; Zhang, Y.; Zhang, J.-G. Lithium metal anodes for rechargeable batteries. *Energy Environ. Sci.* **2014**, *7*, 513−537.

(4) Albertus, P.; Babinec, S.; Litzelman, S.; Newman, A. Status and challenges in enabling the lithium metal electrode for high-energy and low-cost rechargeable batteries. *Nat. Energy* **2018**, *3*, 16−21.

(5) Liu, K.; Pei, A.; Lee, H. R.; Kong, B.; Liu, N.; Lin, D.; Liu, Y.; Liu, C.; Hsu, P.-C.; Bao, Z.; Cui, Y. Lithium Metal Anodes with an Adaptive "Solid-Liquid" Interfacial Protective Layer. *J. Am. Chem. Soc.* **2017**, *139*, 4815−4820.

(6) Shi, F.; Pei, A.; Boyle, D. T.; Xie, J.; Yu, X.; Zhang, X.; Cui, Y. Lithium metal stripping beneath the solid electrolyte interphase. *Proc. Natl. Acad. Sci. U. S. A.* **2018**, *115*, 8529.

(7) Cheng, X.-B.; Zhang, R.; Zhao, C.-Z.; Wei, F.; Zhang, J.-G.; Zhang, Q. A Review of Solid Electrolyte Interphases on Lithium Metal Anode. *Adv. Sci.* **2016**, *3*, No. 1500213.

(8) Fang, C.; Wang, X.; Meng, Y. S. Key Issues Hindering a Practical Lithium-Metal Anode. *Trends Chem.* **2019**, *1*, 152−158.

(9) Xiao, J. How lithium dendrites form in liquid batteries. *Science* **2019**, *366*, 426.

(10) He, Y.; Ren, X.; Xu, Y.; Engelhard, M. H.; Li, X.; Xiao, J.; Liu, J.; Zhang, J.-G.; Xu, W.; Wang, C. Origin of lithium whisker formation and growth under stress. *Nat. Nanotechnol.* **2019**, *14*, 1042−1047.

(11) Liu, J.; Bao, Z.; Cui, Y.; Dufek, E. J.; Goodenough, J. B.; Khalifah, P.; Li, Q.; Liaw, B. Y.; Liu, P.; Manthiram, A.; Meng, Y. S.; Subramanian, V. R.; Toney, M. F.; Viswanathan, V. V.; Whittingham, M. S.; Xiao, J.; Xu, W.; Yang, J.; Yang, X.-Q.; Zhang, J.-G. Pathways for practical high-energy long-cycling lithium metal batteries. *Nat. Energy* **2019**, *4*, 180−186.

(12) Monroe, C.; Newman, J. The Impact of Elastic Deformation on Deposition Kinetics at Lithium/Polymer Interfaces. *J. Electrochem. Soc.* **2005**, *152*, A396.

(13) Monroe, C.; Newman, J. The Effect of Interfacial Deformation on Electrodeposition Kinetics. *J. Electrochem. Soc.* **2004**, *151*, A880.

(14) Ahmad, Z.; Hong, Z.; Viswanathan, V. Design rules for liquid crystalline electrolytes for enabling dendrite-free lithium metal batteries. *Proc. Natl. Acad. Sci. U. S. A.* **2020**, *117*, 26672.

(15) Albertus, P.; Anandan, V.; Ban, C.; Balsara, N.; Belharouak, I.; Buettner-Garrett, J.; Chen, Z.; Daniel, C.; Doeff, M.; Dudney, N. J.; Dunn, B.; Harris, S. J.; Herle, S.; Herbert, E.; Kalnaus, S.; Libera, J. A.; Lu, D.; Martin, S.; McCloskey, B. D.; McDowell, M. T.; Meng, Y. S.; Nanda, J.; Sakamoto, J.; Self, E. C.; Tepavcevic, S.; Wachsman, E.; Wang, C.; Westover, A. S.; Xiao, J.; Yersak, T. Challenges for and Pathways toward Li-Metal-Based All-Solid-State Batteries. *ACS Energy Lett.* **2021**, *6*, 1399−1404.

(16) Park, S.; Jin, H.-J.; Yun, Y. S. Lithium-Metal Anodes: Advances in the Design of 3D-Structured Electrode Materials for Lithium-Metal Anodes (Adv. Mater. 51/2020). *Adv. Mater.* **2020**, *32*, No. 2070386.

(17) Li, S.; Wang, H.; Cuthbert, J.; Liu, T.; Whitacre, J. F.; Matyjaszewski, K. A Semiliquid Lithium Metal Anode. *Joule* **2019**, *3*, 1637−1646.

(18) Liu, H.; Yue, X.; Xing, X.; Yan, Q.; Huang, J.; Petrova, V.; Zhou, H.; Liu, P. A scalable 3D lithium metal anode. *Energy Storage Mater.* **2019**, *16*, 505−511.

(19) Liang, Z.; Lin, D.; Zhao, J.; Lu, Z.; Liu, Y.; Liu, C.; Lu, Y.; Wang, H.; Yan, K.; Tao, X.; Cui, Y. Composite lithium metal anode by melt infusion of lithium into a 3D conducting scaffold with lithiophilic coating. *Proc. Natl. Acad. Sci. U. S. A.* **2016**, *113*, 2862.

(20) Chen, H.; Yang, Y.; Boyle, D. T.; Jeong, Y. K.; Xu, R.; de Vasconcelos, L. S.; Huang, Z.; Wang, H.; Wang, H.; Huang, W.; Li, H.; Wang, J.; Gu, H.; Matsumoto, R.; Motohashi, K.; Nakayama, Y.; Zhao, K.; Cui, Y. Free-standing ultrathin lithium metal−graphene oxide host foils with controllable thickness for lithium batteries. *Nat. Energy* **2021**, *6*, 790−798.

(21) Cheng, Y.; Chen, J.; Chen, Y.; Ke, X.; Li, J.; Yang, Y.; Shi, Z. Lithium Host:Advanced architecture components for lithium metal anode. *Energy Storage Mater.* **2021**, *38*, 276−298.

(22) Wang, H.; Wu, J.; Yuan, L.; Li, Z.; Huang, Y. Stable Lithium Metal Anode Enabled by 3D Soft Host. *ACS Appl. Mater. Interfaces* **2020**, *12*, 28337−28344.

(23) Lorandi, F.; Liu, T.; Fantin, M.; Manser, J.; Al-Obeidi, A.; Zimmerman, M.; Matyjaszewski, K.; Whitacre, J. F. Comparative performance of ex situ artificial solid electrolyte interphases for Li metal batteries with liquid electrolytes. *iScience* **2021**, *24*, No. 102578.

(24) Li, S.; Liu, T.; Yan, J.; Flum, J.; Wang, H.; Lorandi, F.; Wang, Z.; Fu, L.; Hu, L.; Zhao, Y.; Yuan, R.; Sun, M.; Whitacre, J. F.; Matyjaszewski, K. Grafting polymer from oxygen-vacancy-rich nanoparticles to enable protective layers for stable lithium metal anode. *Nano Energy* **2020**, *76*, No. 105046.

(25) Lee, S. H.; Hwang, J.-Y.; Ming, J.; Kim, H.; Jung, H.-G.; Sun, Y.-K. Long-Lasting Solid Electrolyte Interphase for Stable Li-Metal Batteries. *ACS Energy Lett.* **2021**, *6*, 2153−2161.
(26) Cheng, X.-B.; Yan, C.; Chen, X.; Guan, C.; Huang, J.-Q.; Peng, H.-J.; Zhang, R.; Yang, S.-T.; Zhang, Q. Implantable Solid Electrolyte Interphase in Lithium-Metal Batteries. *Chem* **2017**, *2*, 258−270.
(27) Gao, Y.; Yan, Z.; Gray, J. L.; He, X.; Wang, D.; Chen, T.; Huang, Q.; Li, Y. C.; Wang, H.; Kim, S. H.; Mallouk, T. E.; Wang, D. Polymer−inorganic solid−electrolyte interphase for stable lithium metal batteries under lean electrolyte conditions. *Nat. Mater.* **2019**, *18*, 384−389.
(28) Han, B.; Feng, D.; Li, S.; Zhang, Z.; Zou, Y.; Gu, M.; Meng, H.; Wang, C.; Xu, K.; Zhao, Y.; Zeng, H.; Wang, C.; Deng, Y. Self-Regulated Phenomenon of Inorganic Artificial Solid Electrolyte Interphase for Lithium Metal Batteries. *Nano Lett.* **2020**, *20*, 4029−4037.
(29) Li, S.; Lorandi, F.; Wang, H.; Liu, T.; Whitacre, J. F.; Matyjaszewski, K. Functional polymers for lithium metal batteries. *Prog. Polym. Sci.* **2021**, *122*, No. 101453.
(30) Li, S.; Lorandi, F.; Whitacre, J. F.; Matyjaszewski, K. Polymer Chemistry for Improving Lithium Metal Anodes. *Macromol. Chem. Phys.* **2020**, *221*, No. 1900379.
(31) Qian, J.; Henderson, W. A.; Xu, W.; Bhattacharya, P.; Engelhard, M.; Borodin, O.; Zhang, J.-G. High rate and stable cycling of lithium metal anode. *Nat. Commun.* **2015**, *6*, 6362.
(32) Suo, L.; Xue, W.; Gobet, M.; Greenbaum, S. G.; Wang, C.; Chen, Y.; Yang, W.; Li, Y.; Li, J. Fluorine-donating electrolytes enable highly reversible 5-V-class Li metal batteries. *Proc. Natl. Acad. Sci. U. S. A.* **2018**, *115*, 1156.
(33) Zhang, S.; Yang, G.; Liu, Z.; Li, X.; Wang, X.; Chen, R.; Wu, F.; Wang, Z.; Chen, L. Competitive Solvation Enhanced Stability of Lithium Metal Anode in Dual-Salt Electrolyte. *Nano Lett.* **2021**, *21*, 3310−3317.
(34) Ren, X.; Chen, S.; Lee, H.; Mei, D.; Engelhard, M. H.; Burton, S. D.; Zhao, W.; Zheng, J.; Li, Q.; Ding, M. S.; Schroeder, M.; Alvarado, J.; Xu, K.; Meng, Y. S.; Liu, J.; Zhang, J.-G.; Xu, W. Localized High-Concentration Sulfone Electrolytes for High-Efficiency Lithium-Metal Batteries. *Chem* **2018**, *4*, 1877−1892.
(35) Suo, L.; Hu, Y.-S.; Li, H.; Armand, M.; Chen, L. A new class of Solvent-in-Salt electrolyte for high-energy rechargeable metallic lithium batteries. *Nat. Commun.* **2013**, *4*, 1481.
(36) Bachman, J. C.; Muy, S.; Grimaud, A.; Chang, H.-H.; Pour, N.; Lux, S. F.; Paschos, O.; Maglia, F.; Lupart, S.; Lamp, P.; Giordano, L.; Shao-Horn, Y. Inorganic Solid-State Electrolytes for Lithium Batteries: Mechanisms and Properties Governing Ion Conduction. *Chem. Rev.* **2016**, *116*, 140−162.
(37) Manthiram, A.; Yu, X.; Wang, S. Lithium battery chemistries enabled by solid-state electrolytes. *Nat. Rev. Mater.* **2017**, *2*, 16103.
(38) Zhao, Q.; Stalin, S.; Zhao, C.-Z.; Archer, L. A. Designing solid-state electrolytes for safe, energy-dense batteries. *Nat. Rev. Mater.* **2020**, *5*, 229−252.
(39) Choudhury, S.; Stalin, S.; Vu, D.; Warren, A.; Deng, Y.; Biswal, P.; Archer, L. A. Solid-state polymer electrolytes for high-performance lithium metal batteries. *Nat. Commun.* **2019**, *10*, 4398.
(40) Ping, W.; Wang, C.; Wang, R.; Dong, Q.; Lin, Z.; Brozena, A. H.; Dai, J.; Luo, J.; Hu, L. Printable, high-performance solid-state electrolyte films. *Sci. Adv.* **2020**, *6*, No. eabc8641.
(41) Ahmad, Z.; Xie, T.; Maheshwari, C.; Grossman, J. C.; Viswanathan, V. Machine Learning Enabled Computational Screening of Inorganic Solid Electrolytes for Suppression of Dendrite Formation in Lithium Metal Anodes. *ACS Cent. Sci.* **2018**, *4*, 996−1006.
(42) Zhu, Y.; Pande, V.; Li, L.; Wen, B.; Pan, M. S.; Wang, D.; Ma, Z.-F.; Viswanathan, V.; Chiang, Y.-M. Design principles for self-forming interfaces enabling stable lithium-metal anodes. *Proc. Natl. Acad. Sci. U. S. A.* **2020**, No. 202001923.
(43) Kim, M. S.; Ryu, J.-H.; Deepika; Lim, Y. R.; Nah, I. W.; Lee, K.-R.; Archer, L. A.; Il Cho, W. Langmuir−Blodgett artificial solid-electrolyte interphases for practical lithium metal batteries. *Nat. Energy* **2018**, *3*, 889−898.
(44) Xu, N.; Li, L.; He, Y.; Tong, Y.; Lu, Y. Understanding the molecular mechanism of lithium deposition for practical high-energy lithium-metal batteries. *J. Mater. Chem. A* **2020**, *8*, 6229−6237.
(45) Park, S. H.; Jun, D.; Lee, G. H.; Lee, S. G.; Lee, Y. J. Toward high-performance anodeless batteries based on controlled lithium metal deposition: a review. *J. Mater. Chem. A* **2021**, *9*, 14656−14681.
(46) Wang, D.; Liu, H.; Liu, F.; Ma, G.; Yang, J.; Gu, X.; Zhou, M.; Chen, Z. Phase-Separation-Induced Porous Lithiophilic Polymer Coating for High-Efficiency Lithium Metal Batteries. *Nano Lett.* **2021**, *21*, 4757−4764.
(47) Li, N.; Ye, Q.; Zhang, K.; Yan, H.; Shen, C.; Wei, B.; Xie, K. Normalized Lithium Growth from the Nucleation Stage for Dendrite-Free Lithium Metal Anodes. *Angew. Chem., Int. Ed.* **2019**, *58*, 18246−18251.
(48) Liang, X.; Pang, Q.; Kochetkov, I. R.; Sempere, M. S.; Huang, H.; Sun, X.; Nazar, L. F. A facile surface chemistry route to a stabilized lithium metal anode. *Nat. Energy* **2017**, *2*, 17119.
(49) Liu, S.; Zhang, X.; Li, R.; Gao, L.; Luo, J. Dendrite-free Li metal anode by lowering deposition interface energy with Cu99Zn alloy coating. *Energy Storage Mater.* **2018**, *14*, 143−148.
(50) Liu, T.; Hu, Q.; Li, X.; Tan, L.; Yan, G.; Wang, Z.; Guo, H.; Liu, Y.; Wu, Y.; Wang, J. Lithiophilic Ag/Li composite anodes via a spontaneous reaction for Li nucleation with a reduced barrier. *J. Mater. Chem. A* **2019**, *7*, 20911−20918.
(51) Wan, M.; Kang, S.; Wang, L.; Lee, H.-W.; Zheng, G. W.; Cui, Y.; Sun, Y. Mechanical rolling formation of interpenetrated lithium metal/lithium tin alloy foil for ultrahigh-rate battery anode. *Nat. Commun.* **2020**, *11*, 829.
(52) Zhou, Y.; Zhang, J.; Zhao, K.; Ma, Y.; Zhang, H.; Song, D.; Shi, X.; Zhang, L.; Ding, Y. A novel dual-protection interface based on gallium-lithium alloy enables dendrite-free lithium metal anodes. *Energy Storage Mater.* **2021**, *39*, 403−411.
(53) Pande, V.; Viswanathan, V. Computational Screening of Current Collectors for Enabling Anode-Free Lithium Metal Batteries. *ACS Energy Lett.* **2019**, *4*, 2952−2959.
(54) Wang, X.; Zeng, W.; Hong, L.; Xu, W.; Yang, H.; Wang, F.; Duan, H.; Tang, M.; Jiang, H. Stress-driven lithium dendrite growth mechanism and dendrite mitigation by electroplating on soft substrates. *Nat. Energy* **2018**, *3*, 227−235.
(55) Fang, Y.; Zhang, S. L.; Wu, Z.-P.; Luan, D.; Lou, X. W. A highly stable lithium metal anode enabled by Ag nanoparticle−embedded nitrogen-doped carbon macroporous fibers. *Sci. Adv.* **2021**, *7*, No. eabg3626.
(56) Pu, J.; Li, J.; Shen, Z.; Zhong, C.; Liu, J.; Ma, H.; Zhu, J.; Zhang, H.; Braun, P. V. Interlayer Lithium Plating in Au Nanoparticles Pillared Reduced Graphene Oxide for Lithium Metal Anodes. *Adv. Funct. Mater.* **2018**, *28*, No. 1804133.
(57) Jiang, Z.; Jin, L.; Han, Z.; Hu, W.; Zeng, Z.; Sun, Y.; Xie, J. Facile Generation of Polymer−Alloy Hybrid Layers for Dendrite-Free Lithium-Metal Anodes with Improved Moisture Stability. *Angew. Chem., Int. Ed.* **2019**, *58*, 11374−11378.
(58) Malakooti, M. H.; Bockstaller, M. R.; Matyjaszewski, K.; Majidi, C. Liquid metal nanocomposites. *Nanoscale Adv.* **2020**, *2*, 2668−2677.
(59) Dickey, M. D.; Chiechi, R. C.; Larsen, R. J.; Weiss, E. A.; Weitz, D. A.; Whitesides, G. M. Eutectic Gallium-Indium (EGaIn): A Liquid Metal Alloy for the Formation of Stable Structures in Microchannels at Room Temperature. *Adv. Funct. Mater.* **2008**, *18*, 1097−1104.
(60) Wu, Y.; Huang, L.; Huang, X.; Guo, X.; Liu, D.; Zheng, D.; Zhang, X.; Ren, R.; Qu, D.; Chen, J. A room-temperature liquid metal-based self-healing anode for lithium-ion batteries with an ultra-long cycle life. *Energy Environ. Sci.* **2017**, *10*, 1854−1861.
(61) Zhai, P.; Liu, L.; Wei, Y.; Zuo, J.; Yang, Z.; Chen, Q.; Zhao, F.; Zhang, X.; Gong, Y. Self-Healing Nucleation Seeds Induced Long-Term Dendrite-Free Lithium Metal Anode. *Nano Lett.* **2021**, *21*, 7715−7723.
(62) Yan, J.; Malakooti, M. H.; Lu, Z.; Wang, Z.; Kazem, N.; Pan, C.; Bockstaller, M. R.; Majidi, C.; Matyjaszewski, K. Solution processable liquid metal nanodroplets by surface-initiated atom transfer radical polymerization. *Nat. Nanotechnol.* **2019**, *14*, 684−690.

(63) Zhang, S.; Liu, Y.; Fan, Q.; Zhang, C.; Zhou, T.; Kalantar-Zadeh, K.; Guo, Z. Liquid metal batteries for future energy storage. *Energy Environ. Sci.* **2021**, *14*, 4177−4202.

(64) Park, R. J. Y.; Eschler, C. M.; Fincher, C. D.; Badel, A. F.; Guan, P.; Pharr, M.; Sheldon, B. W.; Carter, W. C.; Viswanathan, V.; Chiang, Y.-M. Semi-solid alkali metal electrodes enabling high critical current densities in solid electrolyte batteries. *Nat. Energy* **2021**, *6*, 314−322.

(65) Guo, X.; Ding, Y.; Xue, L.; Zhang, L.; Zhang, C.; Goodenough, J. B.; Yu, G. A Self-Healing Room-Temperature Liquid-Metal Anode for Alkali-Ion Batteries. *Adv. Funct. Mater.* **2018**, *28*, No. 1804649.

(66) Ding, Y.; Guo, X.; Yu, G. Next-Generation Liquid Metal Batteries Based on the Chemistry of Fusible Alloys. *ACS Cent. Sci.* **2020**, *6*, 1355−1366.

(67) Guo, X.; Zhang, L.; Ding, Y.; Goodenough, J. B.; Yu, G. Room-temperature liquid metal and alloy systems for energy storage applications. *Energy Environ. Sci.* **2019**, *12*, 2605−2619.

(68) Lopez, J.; Pei, A.; Oh, J. Y.; Wang, G.-J. N.; Cui, Y.; Bao, Z. Effects of Polymer Coatings on Electrodeposited Lithium Metal. *J. Am. Chem. Soc.* **2018**, *140*, 11735−11744.

(69) Wei, Q.; Sun, M.; Wang, Z.; Yan, J.; Yuan, R.; Liu, T.; Majidi, C.; Matyjaszewski, K. Surface Engineering of Liquid Metal Nanodroplets by Attachable Diblock Copolymers. *ACS Nano* **2020**, *14*, 9884−9893.

(70) Matyjaszewski, K. Atom Transfer Radical Polymerization (ATRP): Current Status and Future Perspectives. *Macromolecules* **2012**, *45*, 4015−4039.

(71) Coessens, V.; Pintauer, T.; Matyjaszewski, K. Functional polymers by atom transfer radical polymerization. *Prog. Polym. Sci.* **2001**, *26*, 337−377.

(72) Matyjaszewski, K.; Xia, J. Atom Transfer Radical Polymerization. *Chem. Rev.* **2001**, *101*, 2921−2990.

(73) Matyjaszewski, K.; Jakubowski, W.; Min, K.; Tang, W.; Huang, J.; Braunecker, W. A.; Tsarevsky, N. V. Diminishing catalyst concentration in atom transfer radical polymerization with reducing agents. *Proc. Natl. Acad. Sci. U. S. A.* **2006**, *103*, 15309.

(74) Wang, Y.; Lorandi, F.; Fantin, M.; Chmielarz, P.; Isse, A. A.; Gennaro, A.; Matyjaszewski, K. Miniemulsion ARGET ATRP via Interfacial and Ion-Pair Catalysis: From ppm to ppb of Residual Copper. *Macromolecules* **2017**, *50*, 8417−8425.

(75) Jakubowski, W.; Matyjaszewski, K. Activators Regenerated by Electron Transfer for Atom-Transfer Radical Polymerization of (Meth)acrylates and Related Block Copolymers. *Angew. Chem., Int. Ed.* **2006**, *45*, 4482−4486.

(76) Wang, Y.; Matyjaszewski, K. Catalytic Halogen Exchange in Miniemulsion ARGET ATRP: A Pathway to Well-Controlled Block Copolymers. *Macromol. Rapid Commun.* **2020**, *41*, No. 2000264.

(77) Taylor, A. Practical surface analysis, 2nd edn., vol I, auger and X-ray photoelectron spectroscopy. Edited by D. Briggs & M. P. Seah, John Wiley, New York, 1990, 657 pp., price: £86.50. ISBN 0471 92081 9. *J. Chem. Technol. Biotechnol.* **1992**, *53*, 215−215.

(78) Huang, C.; Wang, X.; Cao, Q.; Zhang, D.; Jiang, J.-Z. A Self-Healing Anode for Li-Ion Batteries by Rational Interface Modification of Room-Temperature Liquid Metal. *ACS Appl. Energy Mater.* **2021**, *4*, 12224−12231.

(79) Enkovaara, J.; Rostgaard, C.; Mortensen, J. J.; Chen, J.; Dułak, M.; Ferrighi, L.; Gavnholt, J.; Glinsvad, C.; Haikola, V.; Hansen, H. A.; Kristoffersen, H. H.; Kuisma, M.; Larsen, A. H.; Lehtovaara, L.; Ljungberg, M.; Lopez-Acevedo, O.; Moses, P. G.; Ojanen, J.; Olsen, T.; Petzold, V.; Romero, N. A.; Stausholm-Møller, J.; Strange, M.; Tritsaris, G. A.; Vanin, M.; Walter, M.; Hammer, B.; Häkkinen, H.; Madsen, G. K. H.; Nieminen, R. M.; Nørskov, J. K.; Puska, M.; Rantala, T. T.; Schiøtz, J.; Thygesen, K. S.; Jacobsen, K. W. Electronic structure calculations with GPAW: a real-space implementation of the projector augmented-wave method. *J. Phys.: Condens. Matter* **2010**, *22*, No. 253202.

(80) Perdew, J. P.; Burke, K.; Ernzerhof, M. Generalized Gradient Approximation Made Simple. *Phys. Rev. Lett.* **1996**, *77*, 3865−3868.

(81) Das, D.; Chandrasekaran, A.; Venkatram, S.; Ramprasad, R. Effect of Crystallinity on Li Adsorption in Polyethylene Oxide. *Chem. Mater.* **2018**, *30*, 8804−8810.